Spatiotemporal variations of temperature in Jupiter's upper atmosphere

The Planetary Science Journal, 6:92 (9pp), 2025 April https://doi.org/10.3847/PSJ/adc09b

Spatiotemporal Variations of Temperature in Jupiter's Upper Atmosphere

Kate Roberts[1,5], Luke Moore[1,2], James O'Donoghue[3], Henrik Melin[4], Tom Stallard[4], Katie L. Knowles[4], Carl Schmidt[1,2], and Paola I. Tiranti[4]
[1] Department of Astronomy, Boston University, Boston, MA, USA
[2] Center for Space Physics, Boston University, Boston, MA, USA
[3] Department of Meteorology, University of Reading, Reading, UK
[4] Department of Physics, Mathematics & Electrical Engineering, Northumbria University, Newcastle upon Tyne, UK
Received 2024 October 15; revised 2025 February 20; accepted 2025 March 12; published 2025 April 15

Abstract

Global temperatures in Jupiter's upper atmosphere are poorly constrained. Other than an in situ measurement by the Galileo Probe, all temperature data come from remote-sensing methods that primarily rely on emissions from H_3^+, the dominant molecular ion in giant planet ionospheres. While H_3^+ temperature serves as a proxy for thermospheric temperature under specific conditions, the available H_3^+ observations at Jupiter have limited spatial coverage and a wide range of reported temperatures that complicate analysis of atmospheric temperatures. We present high-resolution H_3^+ temperature maps near local solar noon collected over 3 half-nights in 2022 and 2023. Pole-to-pole temperature structure is consistent across time spans of 1 month to 1 yr. Median equatorial ($\pm 25^\circ$ latitude) temperature across all three nights is 762 ± 43 K, with night-to-night differences of <75 K. Temperatures within the statistical locations of the northern and southern auroral ovals are 1200 ± 96 K and 1143 ± 120 K, respectively. A region $\sim$30 K cooler than its surroundings is found near 20° N, 90° W System III longitude, roughly coincident with a magnetic field anomaly, providing additional evidence for magnetic influence on Jupiter's upper atmosphere. Temperatures generally decrease smoothly from auroral to equatorial latitudes, consistent with the expected gradient if Jupiter's nonauroral latitudes are heated primarily by dynamical redistribution of auroral energy.

Unified Astronomy Thesaurus concepts: Jupiter (873); Ground-based astronomy (686); Infrared spectroscopy (2285); Planetary ionospheres (2185)

Materials only available in the online version of record: animation, data behind figures

1. Introduction

Nonauroral temperatures in solar system giant planet upper atmospheres are observed to be significantly hotter than anticipated based on solar extreme ultraviolet (EUV) heating rates. Possible nonsolar sources of energy that may explain observed equatorial temperatures include nonauroral energetic particle precipitation, dissipation of upward-propagating gravity waves, and global redistribution of auroral energy (topics reviewed in R. V. Yelle & S. Miller 2004, Section 9.3.3). There are various complications associated with these additional energy sources though; each would leave a unique spatiotemporal signature in global temperatures if present. Upper-atmospheric dynamics are controlled by temperature gradients, and strong constraints on temperature variations are essential to inform simulation energy inputs. Without them, predictions of giant planet general circulation and atmospheric evolution are limited.

At Jupiter, this temperature discrepancy was first noticed more than 50 yr ago (W. Hubbard et al. 1972; D. F. Strobel & G. R. Smith 1973). Subsequent studies have been mostly inconclusive in identifying the source(s) of additional nonsolar heating. As summarized by R. V. Yelle & S. Miller (2004), early theoretical treatments of gravity waves at Jupiter were highly idealized and could lead to a net heating or cooling in the thermosphere. A more recent treatment demonstrated that waves with properties consistent with those observed by Galileo and New Horizons can provide substantial upper-atmospheric heating when gravity wave energy dissipation via rovibrational damping was included (Y. Lian & R. V. Yelle 2019). There have been only a few general circulation models (GCMs) of Jupiter's upper atmosphere, and those, too, reach inconsistent conclusions regarding the heightened equatorial temperatures. For example, the Jupiter Thermospheric GCM was able to dynamically heat the equatorial thermosphere to observed values when applying a parameterized auroral heating input (S. W. Bougher et al. 2005). However, nonauroral temperatures were too large when a low-latitude particle "drizzle" parameterization was also included, consistent with a lack of convincing evidence for such precipitation. On the other hand, subsequent azimuthally symmetric (C. G. A. Smith & A. D. Aylward 2009) and fully 3D (J. N. Yates et al. 2020) Jupiter GCMs that also included magnetospheric coupling found that auroral energy was largely constrained to high latitude by the strong Coriolis forces, which turn equatorward winds westward.

Observed temperatures have similarly been too limited in scope to provide comprehensive constraints to date. An ionospheric hot spot was found above the Great Red Spot (GRS), possibly a signature of active wave heating (J. O'Donoghue et al. 2016), but evidence for other such hot spots is sparse, and many observations do not see evidence of localized hot spots at the GRS at all (H. Melin et al. 2024). The closest "full-planet" coverage is a map in H. A. Lam et al. (1997), which was ahead of its time in terms of improved global observational coverage, but was unevenly

[5] Corresponding author.

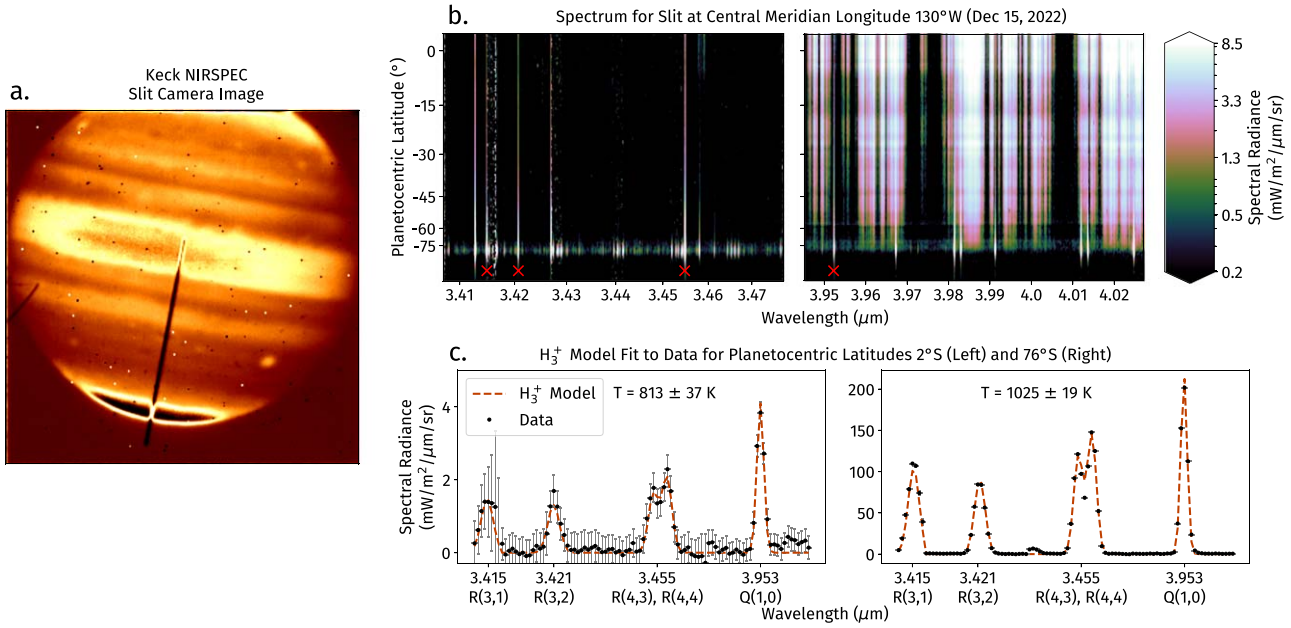

Figure 1. (a) Jupiter on 2022 December 15 as seen through the NIRSPEC slit camera (SCAM) and shortpass filter (1–2.5 μm). The black slit is aligned along the planet's central meridian, where it passes through the equator and southern aurora before hanging over the southern limb. (b) Two orders of a single 2D spectrum corresponding to the SCAM image. We have marked the H_3^+ emission lines used in model fitting with red crosses. Along the vertical axis, notice the brightening of many H_3^+ emissions as they approach the aurora around 75° S. There are a number of other H_3^+ emissions that were not used in the model fitting, primarily due to telluric and/or methane contamination at nonauroral latitudes. (c) Two example h3ppy (H. Melin 2025) H_3^+ spectral extractions and model fits at the equator (left) and aurora (right) from the same data as the spectrum above. Uncertainties on the data are propagated Poisson noise.

sampled in longitude with low spectral resolution, complicating low-latitude temperature retrievals. Constraints on global temporal variations are once again limited. J. O'Donoghue et al. (2021) contains 2 half-nights of observation covering roughly the same magnetic longitudes, but 1 night only covers the northern hemisphere. Other observations of Jupiter's upper atmosphere come from a variety of different instruments and span a wide range of temperatures across the planet (500–1600 K) but are difficult to compare on any consistent basis due to limited spatial and/or temporal coverage (S. Miller et al. 2020).

Here, we present new pole-to-pole observations of Jupiter's upper-atmospheric temperature with ∼170° of longitudinal coverage, including 90° of direct overlap across 3 nights from 2022 to 2023 (Section 2). Results from these observations, all taken using the same observatory and instrument, follow from the same data reduction pipeline for consistency, as detailed in Section 3. The final maps shown in Section 4 reveal clear temperature trends, allowing for significantly improved constraints on spatiotemporal low-latitude temperature variations, as discussed in Section 5.

2. Observations

We observed Jupiter using the Keck II Near-Infrared Spectrometer (NIRSPEC; I. S. McLean et al. 1998; E. C. Martin et al. 2018) on 3 half-nights: 2022 December 15, 2023 November 22, and 2023 December 30 UT. We used NIRSPEC's high-resolution mode with the *KL*r filter; this covers wavelengths from 2.134 to 4.228 μm over seven spectral orders (M = 21–27) with an echelle angle of 62.°02 and cross-disperser angle of 33.°56. The 0.″288 x 24″ slit was paired with six coadds, each of approximately 9 s, producing a high spectral resolution ($\lambda/\Delta\lambda = 25{,}000$–$30{,}000$) spectrum. The instrument had a spectral plate scale of 0.″098 pixel^{-1} and a spatial plate scale of 0.″129 pixel^{-1} with a 2048 × 2048 pixel detector, while its slit-viewing camera (SCAM; E. C. Martin et al. 2016) had a plate scale of 0.″157 pixel^{-1} with 256 × 256 pixels and a shortpass filter covering 1.0–2.5 μm. The nights of observation coincided with the 47th, 56th, and 57th close approaches of Jupiter by the NASA orbiter Juno.

To effectively map the northern and southern hemispheres of the planet, we aligned the instrument slit perpendicular to the equator along the planet's central meridian longitude (CML). The 24″ slit covered just over one Jupiter radius as seen in in Figure 1(a). We mapped the longitude by nodding from the northern to southern slit positions while the planet rotated. Sky spectra were taken every five or six frames to correct for telluric contamination.

3. Methods

3.1. Data Reduction

We used the IDL-based reduction package, REDSPEC (L. Prato et al. 2015), to extract and rectify orders containing viable H_3^+ emissions, then performed an initial wavelength calibration using telluric emission lines from sky frames. Nonuniformity across the detector was corrected by flat fielding. The dark current and Earth's atmosphere were accounted for with sky subtractions, wherein sky frames taken in regular intervals throughout the observation were matched by the closest time to the science spectra of Jupiter. We next performed an absolute flux calibration using A0V stars (HD 1160 for 2022 December and HD 13869 for 2023 November/December), which have relatively flat blackbody curves in this wavelength regime, to convert detector counts to physical flux units using the TRDS version of a Kurucz 1993 stellar atmosphere model (P. L. Lim et al. 2013; P. Lim et al. 2015). This process included a correction for flux lost due to

the narrow width of the spectral slit (0.″288), given the point-spread function of the star due to seeing (from the Maunakea Weather Center DIMM instrument: December 2022: 0.″57, November 2023: 1.″42, and December 2023: 1.″13). An example of a resulting 2D spectrum from reduction is shown in Figure 1(b).

3.2. Mapping the Spectral Slit in Latitude and Longitude

The 3 half-nights observed similar ranges of System III west longitude, allowing for comparisons in time of the same region to better judge temporal variability. The CML coverage for each half-night was ∼95°–210° (2022 December), ∼85°–190° (2023 November), and ∼50°–220° (2023 December). This was determined by using NASA Horizons ephemerides to find the CML throughout the time of observation and applying that information in conjunction with SCAM images. The slit geometry on the planet corresponding to each spectrum was determined by using a mapping routine to fit the planetary limb for SCAM images taken concurrently with spectra (Figure 1(a)). We estimate a typical uncertainty of 0–2 pixels in assigning latitude to spectra along the slit (∼0.5° at the equator, ∼4° near the pole). This follows from a number of possible sources, which include telescope motion during the spectral integration (seen in the 6–8 SCAM frames per spectrum), accuracy in limb fitting, and cropping the spectral order from the wider echelle spectrum. This is similar to uncertainties in previous studies (H. Kita et al. 2018).

To plot the data, we determine the System III longitude and planetocentric latitude for the center of each pixel along the slit. H_3^+ temperatures derived from these spectral frames are then combined into 3° by 6° latitude–longitude bins to better present and analyze trends. The values in each bin are weighted by temperature uncertainties using a bootstrap median. Assuming a Gaussian distribution of temperatures within each bin, we resample those temperatures and their uncertainties to take a more comprehensive median. Calculated root mean square error propagation uncertainties results in a median error of 2% for all data, which is representative of the quality of each H_3^+ model fit. Temperature variability, calculated from the standard deviation of temperatures within a bin, yields a median variability of 4% across all data.

3.3. Temperature Calculations

To measure upper-atmospheric temperatures, we observe infrared emissions from the triatomic hydrogen cation, H_3^+, the dominant molecular ion in giant planet ionospheres. When H_3^+ is in local thermodynamic equilibrium (LTE) with the surrounding gas, its kinetic, rotational, and vibrational temperatures are equal, and it acts as an effective proxy of neutral temperature. Early investigation of Jupiter's H_3^+ auroral emissions demonstrated that the ion's upper vibrational levels were being populated by thermal processes (S. Miller et al. 1990; P. Drossart et al. 1993); without spectroscopic information of the H_3^+ ground vibrational state, it was said to then be in quasi-LTE (S. Miller et al. 2020), in particular for the ν_2 fundamental lines in the 3–4 μm window. Subsequent studies indicated that, while the full LTE should hold where neutral densities are $\geqslant 10^{18}$ m^{-3} (S. Miller et al. 2010), quasi-LTE should hold up to altitudes of 800 km above the 1 bar pressure level (H. Melin et al. 2005; C. Tao et al. 2011). The H_3^+ density peak is expected between 300 and 700 km (e.g., A. Egert et al. 2017; L. Kedziora-Chudczer et al. 2017; Y. Nakamura et al. 2022) (temperature-dependent pressure range: 1 mbar–1 μbar, A. Seiff et al. 1997, which is not perfectly representative of all locations on planet). Therefore, H_3^+ rotational temperatures derived here are representative of a column-averaged local neutral temperature that is weighted by the H_3^+ altitude distribution. For a temperature profile similar to that found by the Galileo Probe (A. Seiff et al. 1997), observed H_3^+ temperatures are modeled to be within 5% of the neutral temperature at the top of the atmosphere (L. Moore et al. 2019).

H_3^+ temperatures were calculated using the Python fitting and modeling package, h3ppy (H. Melin 2025). h3ppy uses the L. Neale et al. (1996) H_3^+ line list and the S. Miller et al. (2010) partition function. For this study, we used five H_3^+ emission lines that were available across all nights and free from spectral contamination (Figure 1(c): 3.41489 μm R(3, 1); 3.42072 μm R(3, 2); a doublet at 3.4547 μm R(4, 3) and 3.45484 μm R(4, 4); and 3.9530 μm Q(1, 0); T. Oka 1981). These emissions appear in the 21st and 24th NIRSPEC orders for our grating settings. The uncertainties on the data in Figure 1(c) are calculated from their associated Poisson noise—the staunch difference in emission magnitude means error bars are much smaller in the polar regions than equatorial. Other H_3^+ emissions are visible in Figure 1(b) but were contaminated by telluric and/or methane features across 1 or more nights. Emission lines are cropped in wavelength from the longer spectrum, and a spatial smoothing factor is applied. This smoothing takes the median value of ±3 pixels in the spatial dimension at a given wavelength to improve H_3^+ model fit success. This does not affect the overall median temperatures, but does decrease the standard deviation in a given latitude–longitude bin by ∼5 K. We did not apply this smoothing in or near the aurora as the spatial scale of intensity variations is much more abrupt at high latitude.

4. Results

Figure 2 shows mapped temperatures for each night. The top row provides context for the coverage in latitude and longitude, with each point being the calculated center of each pixel along the spectral slit. The bottom row shows the same data binned to 3° latitude by 6° longitude to more clearly reveal the structure observed in temperature. Each night has been color-coded for figures where the data have been combined; 2022 December is green, 2023 November is red, and 2023 December is purple. The maps also indicate the statistically averaged location of the outer main auroral ovals in solid lines (B. Bonfond et al. 2012). As indicated with a white ellipse on the upper plots, Jupiter's GRS was observed on 2023 November at a CML of 90° and in 2023 December at a CML of 101° (both centered at 19° S latitude); no temperature anomalies are found in those regions, consistent with H. Melin et al. (2024). Equatorial temperature, T_{eq}, trends are quantified here by calculating the median and standard deviation of all temperature values within ±25° of the joviographic equator for all observed longitudes on a given night. T_{eq} decreases from 820 ± 31 K in 2022 December to 751 ± 26 K in 2023 November and 746 ± 23 K in 2023 December. (T_{eq} differences computed only over longitudes sampled on all 3 nights are similar.) This could be consistent with a long-term trend of decreasing temperatures, but this data set is too limited to draw such long-term conclusions.

We also calculate the median and standard deviation of temperature bins strictly within the bounds of the northern (T_N)

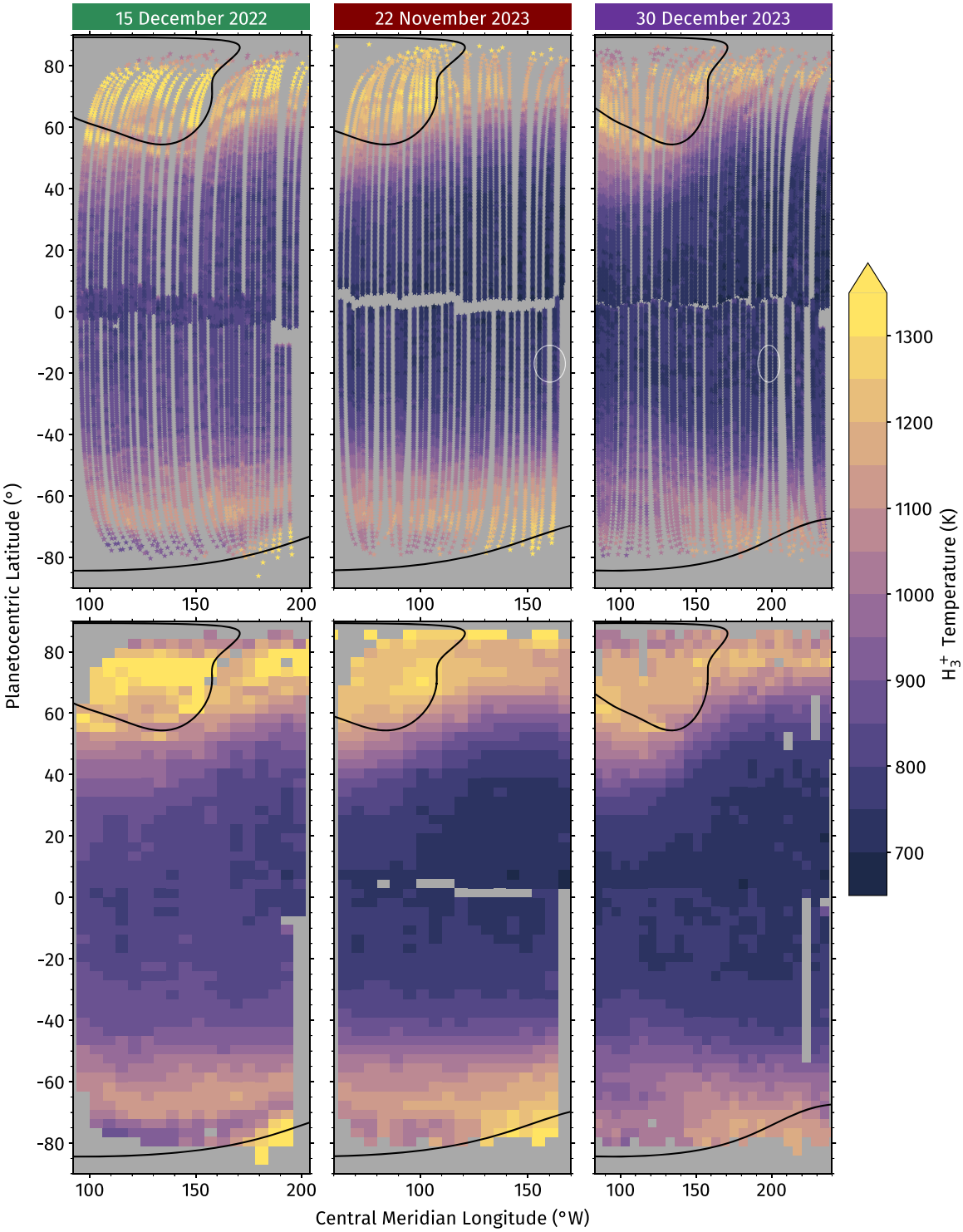

Figure 2. Column-averaged H_3^+ temperature at Jupiter plotted in planetocentric latitude and central meridian longitude (CML). On each plot, the statistically averaged locations of the outer auroral ovals are plotted (B. Bonfond et al. 2012). Top: individual temperature values derived from the center of each pixel along the slit for each night. White ellipses mark the location of the GRS on the 2023 November and December nights. Bottom: the same data binned to 3° latitude by 6° longitude using a bootstrap median. The data behind this figure are available. It contains many csv files for each observation date plus some Python code to read and recreate the figure. (The data used to create this figure are available in the online article.)

and southern (T_S) auroral ovals (i.e., poleward of the solid line at each pole). For 2022 December , $T_N = 1247 \pm 122$ K and $T_S = 1357 \pm 128$ K. For 2023 November, $T_N = 1230 \pm 55$ K and $T_S = 1295 \pm 18$ K. For 2023 December, $T_N = 1163 \pm 56$ K and $T_S = 1130 \pm 62$ K. Due to the southern oval being well centered at the planetographic pole and Jupiter's small obliquity, we have limited coverage of the southern aurora, and thus, these values have been calculated from a small number of temperatures, especially 2022 December, which only has ten observed temperature values. Comparing values from all 3 nights, we observe a median northern temperature of 1200 ± 92 K from 1727 auroral values and a southern

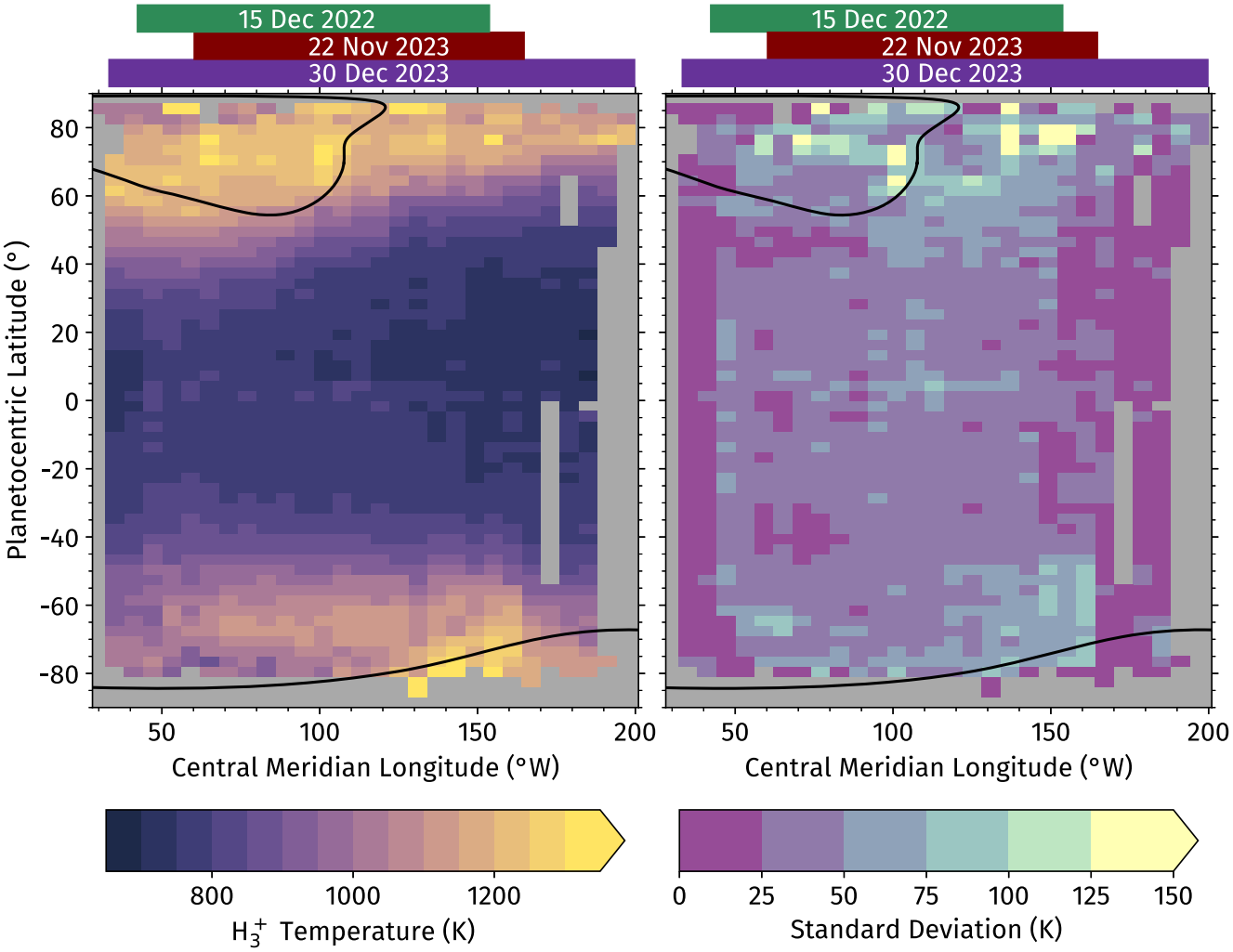

Figure 3. Column-averaged H_3^+ temperature and corresponding standard deviation. Data have been binned to 3° latitude by 6° longitude. Statistically averaged locations of the outer main auroral ovals are shown in solid lines (B. Bonfond et al. 2012), with the longitudinal coverage of each night of observation indicated at the top in green (2022 December), red (2023 November), and purple (2023 December). The data behind this figure are available. It contains a csv file and some Python code to read and recreate the figure.

(The data used to create this figure are available in the online article.)

temperature of 1143 ± 120 K from 96 auroral values. Therefore, there is no clear distinction between northern and southern auroral temperatures, at least within this limited data set.

In Figure 3, data from all 3 nights have been combined into 3° by 6° latitude–longitude bins. The final temperature of a bin is the bootstrap median of all values within the bin that accounts for the associated uncertainties from the model fits. The H_3^+ emission line model fits used to calculate these temperatures have a median root mean square error of 2% and a maximum of 11%, with higher errors at low latitude, as indicated in Figure 1(c). The corresponding standard deviation of the binned temperatures is mapped on the right: the median deviation is 4%, and the maximum is 21%. Along the top of each map are colored bars that denote the longitudinal coverage of each night; following their assigned colors, 2022 December is green, 2023 November is red, and 2023 December is purple. As before, the statistically averaged location of the outer main auroral ovals from B. Bonfond et al. (2012) are shown with solid lines.

In Figure 4, data have been collapsed in longitude to observe latitudinal trends in temperature from night to night. Each night is plotted in its corresponding colors. The standard deviation of all temperatures within each 1° latitude bin is represented in the shaded boundary. From this, the differences between observations become more apparent: 2022 December is significantly hotter in the equatorial region, while the two nights in 2023 agree relatively well. We note the presence of a transient subauroral temperature minimum around 75° S in 2022 December and 2023 November, which is also present but less obvious in Figure 2. We have included an animated version of Figure 4 that shows how latitudinal temperature structure changes over 6° longitude bins for each night of observation.

5. Discussion

5.1. Auroral Energetics and the Role of H_3^+

Observed temperatures here lie within the wide range of previously published values. For the equatorial region, ground-based literature includes typical column-averaged H_3^+ temperatures from 500 K (T. S. Stallard et al. 2017) to 800 K (J. O'Donoghue et al. 2016), while Juno/JIRAM has observed temperatures of

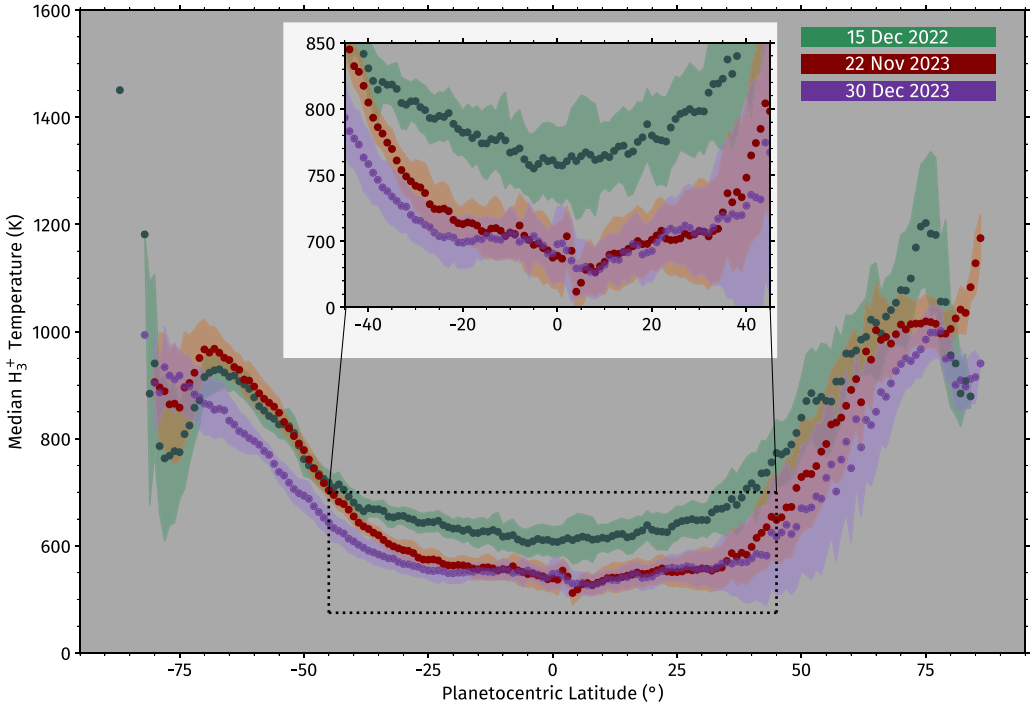

Figure 4. H_3^+ column-averaged temperature profiles for all 3 nights (2022 December in green, 2023 November in red, and 2023 December in purple). These profiles represent the median temperature, binned by 1° in latitude, across all observed longitudes. The inset plot improves visibility for the similarities and differences between the 3 nights at equatorial latitudes. Shaded regions show the standard deviation in each latitude bin. An animation of this figure is available. It shows the changes in the latitudinal temperature structure over 6° longitude bins for each night of observation, with white lines indicating the average latitude of the northern and southern auroral ovals for each longitude bin (B. Bonfond et al. 2012). The animation begins in the 60–80° W bin and runs to the 212–220° W bin. The real-time duration of the animation is 24 s. The data behind this figure are also available. It contains three csv files, one for each observation date, plus some Python code to read and recreate the figure.

(An animation of this figure is available in the online article.)

(The data used to create this figure are available in the online article.)

800 K (A. Migliorini et al. 2019). In the aurora, ground-based observations of northern temperatures range from 650 K (G. E. Ballester et al. 1994; S. Miller et al. 1997) to 1200 K (E. Raynaud et al. 2004), with spacecraft observations spanning 500 K (Galileo/NIMS; F. Altieri et al. 2016) to 1400 K (Cassini/VIMS; T. S. Stallard et al. 2015). For the southern aurora, ground-based observations range from 850 K (H. Kita et al. 2018) to 1250 K (M. B. Lystrup et al. 2008), and spacecraft observations range from 940 K (Juno/JIRAM; A. Adriani et al. 2017) to 1200 K (Cassini/VIMS; T. S. Stallard et al. 2015).

The substantial variation of reported auroral temperatures, and the relatively high auroral temperature variability found here, are reasonable when considering the stochastic nature of those emissions (e.g., S. V. Badman et al. 2015). In addition to spatial and temporal variations of auroral particle precipitation, column-averaged H_3^+ temperatures are also sensitive to the mean energy of any precipitating particles. Whereas the primary difference in ultraviolet (UV) emission with increasing mean energy is that there will be more absorption due to methane and a higher derived color ratio (J. C. Gérard et al. 2023), H_3^+ emission is weighted by its vertical density distribution. For example, precipitating electrons with mean energy of 100 keV would produce enhanced ionization peaking near 300 km altitude (C. Tao et al. 2011; J. C. Gérard et al. 2014), meaning column-averaged H_3^+ temperatures in that region would primarily reflect temperatures near the base of the thermosphere. In contrast, a high-latitude solar-produced ionosphere would generate a relatively high-altitude H_3^+ density peak due to the increased atmosphere path length. Derived temperatures would then be higher for a typical Bates-like profile with a positive thermospheric temperature gradient (e.g., A. Seiff et al. 1997). Alternatively, where auroral heating mechanisms generate low-altitude (400 km, 1 μbar) hot spots as predicted by models (T. Majeed et al. 2009; J. N. Yates et al. 2020), higher-energy precipitation would weight observed H_3^+ emission to the low-altitude, high-temperature regions. In either case, while H_3^+ upper-atmospheric temperatures are observed to be highest on average in the auroral region, their high degree of spatiotemporal variability helps to emphasize that, on their own, they cannot be used to reliably constrain auroral energetics. Additional information, such as altitude profiles of H_3^+ temperature and volumetric number density, is needed to contextualize observed variability.

5.2. Determining a Dominant, Upper-atmospheric Jovian Energy Source

Global temperature trends are in some ways more revealing of the dominant energy source(s) in Jupiter's upper atmosphere. If heating due to upward-propagating, lower-atmospheric waves is significant, there should be localized temperature hot spots above any active regions. We see no such evidence across 3 half-nights of observation, indicating that wave heating is not contributing significantly to the upper-atmospheric energy budget over this period or that perhaps it is a distributed low-level amount of heating. Instead, temperatures peak at high latitude, especially within the statistically averaged auroral oval locations, and decrease steadily toward the equator. This trend is expected if Jupiter's aurorae are the dominant source of upper-atmospheric

heating (e.g., S. W. Bougher et al. 2005; C. Tao et al. 2009). Such a temperature gradient has been seen before at Jupiter (J. O'Donoghue et al. 2021). By demonstrating a repeating temperature gradient over the same range of longitudes across 3 separate nights, these results significantly expand on the observational evidence in support of the notion that Jupiter's nonauroral latitudes are heated primarily by dynamical redistribution of auroral energy.

There are, however, a few exceptions to such a latitudinal trend in the literature. Pole-to-pole H_3^+ temperature measurements by G. E. Ballester et al. (1994) found low-latitude temperature enhancements up to 1200 K near 102° W CML. H. A. Lam et al. (1997) produced (interpolated) global maps of observed H_3^+ parameters and found similar low-latitude hot spots, of order 900 K, at a range of CMLs. More recently, A. Migliorini et al. (2019) derived H_3^+ altitude profiles from Juno/JIRAM limb observations and found that temperatures were generally coolest at mid-latitude and increased toward the equator, while J. O'Donoghue et al. (2016) found a 1600 K hot spot above the GRS.

Taken together, it seems that direct upper-atmospheric heating by upward-propagating waves is, at best, variable. It may lead to localized hot spots, but they appear to be either short-lived, infrequent, or both. In particular, the absence of any nonauroral hot spots on either 2023 November 22 or December 30 (Figure 2) implies that either direct wave heating signatures persist for <38 days, no such "events" occurred over that period in the observed longitude sector, or they are occurring on smaller spatial or temperature scales than we can resolve. Recent JWST/NIRSpec observations revealed evidence of such small-scale wave structure surrounding the GRS (H. Melin et al. 2024). In the meantime, observed temperature gradients demonstrate that the Coriolis barrier responsible for trapping auroral energy at high latitudes in some GCMs must somehow be overcome by Jupiter. A similar temperature trend was derived from UV occultations at Saturn (Z. Brown et al. 2020), where zonal drag due to atmospheric gravity waves—seen both in remote temperature profiles and in situ Cassini measurements—was used to enable equatorward redistribution of auroral energy in a Saturn GCM (I. C. Müller-Wodarg et al. 2019). Therefore, while it is clear that waves are present in giant planet thermospheres, their primary contribution to upper-atmospheric heating may be in modifying dynamics. In that scenario, prior observations of infrequent nonauroral H_3^+ temperature hot spots might be evidence that, while upward-propagating waves may impart ephemeral heating, they do not contribute significantly to the long-term energy budget of Jupiter's low-latitude upper atmosphere.

5.3. A Longitudinal Anomaly

Beyond just a monotonic decrease in H_3^+ temperature from polar-to-equatorial latitudes, these maps reveal a possible organization of temperature with System III West longitude and thus, magnetic field. For these observations the spectral slit was centered along the central meridian, so they are all fixed near the local solar noon. Yet, even on a single night of observing, individual noon equatorial (±25°) temperature measurements are observed to vary by more than 200 K as a function of CML (as seen in the top panels of Figure 2). In simulations, neutral winds diverging from the auroral region are rapidly turned westward by strong Coriolis forces, meaning the mid- to low-latitude thermosphere is expected to exhibit strong zonal winds (decreasing with latitude) with minimal variation in longitude/local time. Symmetry created in longitude by zonal winds is strong enough that GCMs present temperatures as zonally averaged, i.e., no temperature structures corresponding to those in Figures 2 and 3 are found even for model results presented in latitude and longitude (e.g., T. Majeed et al. 2009) (though it must be noted that Jupiter GCMs have not yet incorporated JRM33, the Juno-derived magnetic field model that includes finer-scale magnetic field features, e.g., S. W. Bougher et al. 2005; C. Tao et al. 2009; and J. N. Yates et al. (2020). Thus, based on existing simulations, the observed longitudinal temperature variations appear to be unlikely to represent true variations in thermospheric temperature. Due to the nature of H_3^+ temperature retrievals, which are weighted near the H_3^+ density peak in altitude, they might instead be associated with a low-altitude ionospheric region.

To create a region of low-altitude H_3^+ density, we now turn to local electrodynamics and Jupiter's magnetic field. Around 90° W, Jupiter's magnetic field is very complex, possibly related to a magnetic oddity known as the "Great Blue Spot" (K. M. Moore et al. 2018; J. E. Connerney et al. 2022). Associated plasma dynamics are also more complicated within this region of twisted magnetic field. In a perfect dipole, magnetic field lines are oriented perpendicular to the flow of neutral zonal winds. In this region, however, field lines have a more significant zonal component that could cause westward neutral winds to drive plasma down field lines and thus down in altitude, at northern latitudes. This would be consistent with a preferential north–south asymmetry in temperatures near 90° W.

The region of H_3^+ temperature decrease also coincides with H_3^+ emission features found using images and spectra taken more than 20 yrs ago (T. S. Stallard et al. 2018; P. Drossart 2019) as well as a localized "bulge" of enhanced H Lyα emission discovered more than 40 yr ago (J. T. Clarke et al. 1980; B. R. Sandel et al. 1980; H. Melin & T. S. Stallard 2016). T. S. Stallard et al. (2018) presented a global map constructed from thousands of narrowband images that found evidence for localized interactions with Jupiter's magnetic field. Two prominent features stand out from that map: a sinusoidal pattern of weakened H_3^+ emission (known as the "dark ribbon" and shown to track the magnetic equator) and a large region of dimmed H_3^+ emission between ∼60 and 150° W CML, which is coincident with the "Great Blue Spot." H_3^+ being pushed to lower altitudes is an attractive explanation for our observed temperatures as it may also relate to these broader mysteries. Rather than recreating a broad H Lyα line profile in the bulge region (J. T. Clarke et al. 1980) by dissociative recombination of H_3^+ with precipitating electrons (H. Melin & T. S. Stallard 2016), a forced H_3^+ downwelling could cause H_3^+ to charge exchange with methane. This would lead to a chain of hydrocarbon ions, some of which may also produce hot H upon recombination, leading to the broadened line profile observed by J. T. Clarke et al. (1980) and eliminating the need for low-latitude electron precipitation presented in H. Melin & T. S. Stallard (2016). Recombination would also result in a local depletion in electrons, which is present in Galileo radio occultations and Juno in situ data in this region (M. Mendillo et al. 2022; W. Kurth et al. 2025). Given the correspondence of depleted H_3^+ emission, the H Lyα bulge, the unusual magnetic field structure, and now our temperature measurements over

varying timescales at 20° N, 90° W, it seems that these oddities are likely not associated with a variable external driver, such as solar EUV flux or possible low-latitude particle precipitation.

6. Conclusions

We present the first multi-epoch, pole-to-pole high-resolution H_3^+ temperature map as a first step in constraining the temperatures in Jupiter's upper atmosphere. We find a median equatorial (±25°) temperature of $T_{eq} = 762 \pm 43$°K over 3 half-nights of observation covering similar magnetic longitudes separated by time spans of 1 month and 1 yr. While median equatorial temperatures can differ by ∼75 K in 1 yr, they are remarkably consistent otherwise. Median equatorial temperatures vary only by 5 K in just over a month, and the median nonauroral temperature deviation is only 4% across an average of 50 data points in each equatorial latitude–longitude bin.

Observed H_3^+ temperatures decrease from aurora to equator, and we see no evidence for any localized nonauroral hot spots. These smooth global temperature gradients are consistent with the aurorae being the primary source of heating for Jupiter's nonauroral upper atmosphere. In addition, we find that mid- and low-latitude H_3^+ temperatures surrounding the 20° N, 90° W region are systematically cooler (25 K) than those near 180° W. This apparent magnetic control of H_3^+ temperature (and emission, as detected previously) is coterminous with other unusual features at Jupiter, notably the complex magnetic field surrounding the "Great Blue Spot" and the H Lyα bulge.

Future work will focus on expanding this map by coverage in time and space. With a fully global map, we can develop significantly improved constraints on the energetics of Jupiter's upper atmosphere as a whole rather than over a subset of longitudes. By expanding our temporal coverage, we can better understand Jovian temperature variability and its possible drivers.

Acknowledgments

K.R. was supported by NASA FINESST grant 80NSSC23K1637. L.M. and C.S. acknowledge support from NASA's Solar System Observation program via grants 80NSSC22K095 and 80NSSC25K7727. J.O. was supported by the STFC Ernest Rutherford Fellowship ST/X003426/1 at the University of Reading. H.M. was supported by the STFC James Webb Fellowship (ST/W001527/2) at Northumbria University, UK. K.L.K. was supported by a Northumbria University Research Studentship at Northumbria University, UK. P.I.T. was supported by UK Science and Technology Facilities Council (STFC) Studentship ST/X508548/2.

This research was selected under the Key Strategic Mission Support (KSMS) category of NASA's Keck General Observing program which is managed by the NASA Exoplanet Science Institute (NExScI) and funded under the auspices of NASA's Planetary Science Division. Data presented herein were obtained at the W. M. Keck Observatory from telescope time allocated to the National Aeronautics and Space Administration through the agency's scientific partnership with the California Institute of Technology and the University of California. The Observatory was made possible by the generous financial support of the W. M. Keck Foundation. The authors wish to recognize and acknowledge the very significant cultural role and reverence that the summit of Maunakea has always had within the indigenous Hawaiian community. We are most fortunate to have the opportunity to conduct observations from this mountain.

We acknowledge the contribution of the International Space Sciences Institute (ISSI) in Bern, Switzerland, for hosting and funding International Team 23-592 ("Jupiter's Non-Auroral Ionosphere"), and the constructive discussions by colleagues attending that meeting.

Facilities: Keck:II (NIRSPEC).

Software: h3ppy (H. Melin 2025), Astropy (Astropy Collaboration et al. 2013, 2018), pandas (W. McKinney 2010; The pandas development Team 2024), SciPy (P. Virtanen et al. 2020), PySynphot (P. L. Lim et al. 2013, P. Lim et al. 2015), numpy (C. R. Harris et al. 2020), Matplotlib (J. D. Hunter 2007).

ORCID iDs

Kate Roberts https://orcid.org/0000-0002-5753-1262
Luke Moore https://orcid.org/0000-0003-4481-9862
James O'Donoghue https://orcid.org/0000-0002-4218-1191
Henrik Melin https://orcid.org/0000-0001-5971-2633
Tom Stallard https://orcid.org/0000-0003-3990-670X
Katie L. Knowles https://orcid.org/0000-0001-5055-8115
Carl Schmidt https://orcid.org/0000-0002-6917-3458
Paola I. Tiranti https://orcid.org/0000-0001-7339-9495

References

Adriani, A., Mura, A., Moriconi, M. L., et al. 2017, GeoRL, 44, 4633
Altieri, F., Dinelli, B. M., Migliorini, A., et al. 2016, GeoRL, 43, 11558
Astropy Collaboration, Price-Whelan, A. M., Sipőcz, B. M., et al. 2018, AJ, 156, 123
Astropy Collaboration, Robitaille, T. P., Tollerud, E. J., et al. 2013, A&A, 558, A33
Badman, S. V., Branduardi-Raymont, G., Galand, M., et al. 2015, SSRv, 187, 99
Ballester, G. E., Miller, S., Tennyson, J., Trafton, L. M., & Geballe, T. R. 1994, Icar, 107, 189
Bonfond, B., Grodent, D., Gérard, J. C., et al. 2012, GeoRL, 39, L01105
Bougher, S. W., Waite, J. H., Majeed, T., & Gladstone, G. R. 2005, JGRE, 110, E04008
Brown, Z., Koskinen, T., Müller-Wodarg, I., et al. 2020, NatAs, 4, 872
Clarke, J. T., Weaver, H. A., Feldman, P. D., et al. 1980, ApJ, 240, 696
Connerney, J. E., Timmins, S., Oliversen, R. J., et al. 2022, JGRE, 127, e07055
Drossart, P. 2019, RSPTA, 377, 20180404
Drossart, P., Maillard, J. P., Caldwell, J., & Rosenqvist, J. 1993, ApJL, 402, L25
Egert, A., Waite, J. H., & Bell, J. 2017, JGRA, 122, 2210
Gérard, J. C., Bonfond, B., Grodent, D., et al. 2014, JGRA, 119, 9072
Gérard, J. C., Gkouvelis, L., Bonfond, B., et al. 2023, Icar, 389, 115261
Harris, C. R., Millman, K. J., van der Walt, S. J., et al. 2020, Natur, 585, 357
Hubbard, W., Nather, R. E., Evans, D. S., et al. 1972, AJ, 77, 41
Hunter, J. D. 2007, CSE, 9, 90
Kedziora-Chudczer, L., Cotton, D., Kedziora, D., & Bailey, J. 2017, Icar, 294, 156
Kita, H., Fujisawa, S., Tao, C., et al. 2018, Icar, 313, 93
Kurth, W., Faden, J., Waite, J. H., et al. 2025, JGRE, 130, 2024JE008845
Lam, H. A., Achilleos, N., Miller, S., et al. 1997, Icar, 127, 379
Lian, Y., & Yelle, R. V. 2019, Icar, 329, 222
Lim, P. L., Diaz, R. I., & Laidler, V., 2013 pysynphot: Synthetic Photometry Software Package, v2.0.0
Lim, P., Diaz, R., & Laidler, V., 2015 pysynphot: Synthetic Photometry Software Package, Astrophysics Source Code Library, ascl:1303.023
Lystrup, M. B., Miller, S., Russo, N. D., Vervack, R. J., J., & Stallard, T. 2008, ApJ, 677, 790
Majeed, T., Waite, J. H., Bougher, S. W., & Gladstone, G. R. 2009, JGRE, 114, E07005
Martin, E. C., Fitzgerald, M. P., McLean, I. S., Kress, E., & Wang, E. 2016, Proc. SPIE, 9908, 99082R
Martin, E. C., Fitzgerald, M. P., McLean, I. S., et al. 2018, Proc. SPIE, 10702, 107020A

McKinney, W. 2010, in Proc. 9th Python in Science Conf. ed. S. van der Walt & J. Millman, 56
McLean, I. S., Becklin, E. E., Bendiksen, O., et al. 1998, Proc. SPIE, 3354, 566
Melin, H. 2025, JOSS, 10, 7536
Melin, H., Miller, S., Stallard, T., & Grodent, D. 2005, Icar, 178, 97
Melin, H., O'Donoghue, J., Moore, L., et al. 2024, NatAs, 8, 1000
Melin, H., & Stallard, T. S. 2016, Icar, 278, 238
Mendillo, M., Narvaez, C., Moore, L., & Withers, P. 2022, JGRE, 127, e2021JE007169
Migliorini, A., Dinelli, B. M., Moriconi, M. L., et al. 2019, Icar, 329, 132
Miller, S., Achilleos, N., Ballester, G. E., et al. 1997, Icar, 130, 57
Miller, S., Joseph, R. D., & Tennyson, J. 1990, ApJ, 55, L55
Miller, S., Stallard, T., Melin, H., & Tennyson, J. 2010, FaDi, 147, 283
Miller, S., Tennyson, J., Geballe, T. R., & Stallard, T. 2020, RvMP, 92, 035003
Moore, K. M., Yadav, R. K., Kulowski, L., et al. 2018, Natur, 561, 76
Moore, L., Melin, H., O'Donoghue, J., et al. 2019, RSPTA, 377, 20190067
Müller-Wodarg, I. C., Koskinen, T. T., Moore, L., et al. 2019, GeoRL, 46, 2372
Nakamura, Y., Terada, K., Tao, C., et al. 2022, JGRA, 127, e30312
Neale, L., Miller, S., & Tennyson, J. 1996, ApJ, 464, 516
O'Donoghue, J., Moore, L., Stallard, T. S., & Melin, H. 2016, Natur, 536, 190
O'Donoghue, J., Moore, L., Bhakyapaibul, T., et al. 2021, Natur, 596, 54
Oka, T. 1981, RSPTA, 303, 543
Prato, L., Kim, S. S., & McLean, I., 2015 REDSPEC Data Reduction Manual, Astrophysics Source Code Library, ascl:1507.017
Raynaud, E., Lellouch, E., Maillard, J. P., et al. 2004, Icar, 171, 133
Sandel, B. R., Broadfoot, A. L., & Strobel, D. F. 1980, GeoRL, 7, 5
Seiff, A., Kirk, D. B., Knight, T. C. D., et al. 1997, Sci, 276, 102
Smith, C. G. A., & Aylward, A. D. 2009, AnGeo, 27, 199
Stallard, T. S., Burrell, A. G., Melin, H., et al. 2018, NatAs, 2, 773
Stallard, T. S., Melin, H., Miller, S., et al. 2015, JGRA, 120, 6948
Stallard, T. S., Melin, H., Miller, S., et al. 2017, GeoRL, 44, 3000
Strobel, D. F., & Smith, G. R. 1973, JAtS, 30, 718
Tao, C., Badman, S. V., & Fujimoto, M. 2011, Icar, 213, 581
Tao, C., Fujiwara, H., & Kasaba, Y. 2009, JGRA, 114, A08307
The pandas development Team 2024, Pandas-dev/pandas: Pandas, v2.2.2, Zenodo, doi:10.5281/zenodo.10957263
Virtanen, P., Gommers, R., Oliphant, T. E., et al. 2020, NatMe, 17, 261
Yates, J. N., Ray, L. C., Achilleos, N., Witasse, O., & Altobelli, N. 2020, JGRA, 125, e2019JA026792
Yelle, R. V., & Miller, S. 2004, in Jupiter. The Planet, Satellites and Magnetosphere, ed. F. Bagenal, T. E. Dowling, & W. B. McKinnon (Cambridge: Cambridge Univ. Press), 185